Polymorphism in Li 4 Zn(PO 4) 2 and Stabilization of its Structural Disorder to Improve Ionic Conductivity

Sujoy Saha, Gwenaëlle Rousse, Ignacio Blazquez Alcover, Mathieu Courty, Daniel Alves Dalla Corte, Jean-marie Tarascon

Polymorphism in $Li_4Zn(PO_4)_2$ and Stabilization of its Structural Disorder to Improve Ionic Conductivity

Sujoy Saha[†‡§], Gwenaëlle Rousse[†‡§], Ignacio Blazquez Alcover[†§], Mathieu Courty[§⊥], Daniel Alves Dalla Corte[†‡§] and Jean-Marie Tarascon[†‡§*]

[†]Collège de France, Chaire de Chimie du Solide et de l'Energie, UMR 8260, 11 place Marcelin Berthelot, 75231 Paris CEDEX 05, France
[‡] Sorbonne Universités – UPMC Univ Paris 06, 4 place Jussieu, F-75005 Paris, France
[§] Réseau sur le Stockage Electrochimique de l'Energie (RS2E), FR CNRS 3459 – France
[⊥]Laboratoire de Réactivité et Chimie des Solides, Université de Picardie Jules Verne, 33 Rue Saint Leu, 80039 Amiens, France

ABSTRACT

Realization of the vulnerability of current rechargeable battery systems drives the research of solid electrolytes. In the search for a new Li ion conductor, we explore the rich crystal chemistry of $Li_4Zn(PO_4)_2$ which presents a low temperature monoclinic (α-) and a high temperature orthorhombic (β-) polymorph. We solved the crystal structure of the β-phase and found that it has a disordered Li/Zn-sublattice while showing the largest conductivity; however it could not be stabilized at room temperature by quenching. We discovered that the partial substitution of Zn^{2+} with Ga^{3+} in $Li_{4-x}Zn_{1-x}Ga_x(PO_4)_2$ first leads to an intermediate β' phase. Increasing the Ga content to 0.5 mol pfu. enables to stabilize the pure β-phase at room temperature, which exhibits a conductivity by several orders of magnitudes higher than the pristine sample. The crystal structures of the new β'/β- phases have been solved to elucidate the conduction mechanism, which confirms the high sensitivity of ionic conductivity on disorder.

*Corresponding author: Jean-Marie Tarascon: jean-marie.tarascon@college-de-france.fr

INTRODUCTION

Li-ion batteries have become worldwide accepted to power today's portable electronics because they offer high energy density[1–3]. For the same reason, they have become the technology of choice for EV's, but safety concerns associated with the use of flammable liquid electrolytes remain a serious challenge.[4–6] A possible option consists in replacing the liquid electrolytes by their solid counterparts. Finding suitable solid electrolytes having high ionic conductivity will not only enable to design safer 'all-solid-state Li-ion batteries', but will also open new possibilities to play with future-generation battery chemistries like Li-S, Li-Br or Li-air[7–9]. Although solid state electrolytes are known since the observation of

ionic conduction upon heating in Ag_2S and PbF_2 by Faraday in the 1830s,[10] it is only in 1960-80's that they were studied extensively. This fruitful period has seen the discovery of many new Li-ion conducting compound classes, e.g., LISICON, NASICON, LIPON, thio-LISICON etc.; but the conductivities of these solid electrolytes were far behind practical utilization and this research fall into oblivion[11–14]. However, recent safety issues of LIB's and foreseen aspiration of industries has led researchers to re-visit the field intensely in the past decade and several new interesting compounds like garnets, perovskites etc. were found[15,16], but still with conductivities (~10^{-4}-10^{-6} Scm^{-1}) trailing far behind than that of liquid electrolytes[17]. It is only recently, with the discovery of thio-phosphate $Li_{11-x}M_{2-x}P_{1+x}S_{12}$ (M = Si, Ge, Sn) that ionic conductivities comparable to the liquids (~10^{-2}-10^{-3} Scm^{-1}) have been achieved. However, instability issues, synthesis and handling difficulties together with the lack of compatibility with Li-electrode has clogged its practical relevance.[18–20] Owing to their greater stability, ease of handling and larger electrochemical window, oxides are still foreseen best candidates to replace liquid electrolytes, provided an improved ionic conductivity. Hence we concentrate our search towards new Li ionic conducting oxides apart from the exhaustively explored list of above mentioned families.

Phosphates have fascinated chemists for many years, thanks to their stability, rich crystal-chemistry, and partly because of subtle interactions between phosphate framework and mobile Li^+ ions, which accounts for their high ionic conductivities[21–23]. Along this line, we spotted $Li_4Zn(PO_4)_2$ as a potential candidate. Although this compound was reported as early as in 1976, it was never explored in details for its transport properties despite its rich chemistry.[24] This compound received further attention in 1986 by West et *al.*, who explored its thermal stability by differential thermal analysis of Li_3PO_4-$Zn_3(PO_4)_2$ solid solutions.[25] Interestingly, they reported three polymorphs, low temperature the α-$Li_4Zn(PO_4)_2$ and the high temperature β- and γ- $Li_4Zn(PO_4)_2$, and moreover they speculated that the β- phase derives from the α- phase by cation disordering. One year later, the same group, prepared the pure compound by solid state synthesis and explored its ionic conductivity.[26] They found that $Li_4Zn(PO_4)_2$ is a poor Li^+ conductor, but noticed an increase of conductivity for the β-phase. Fifteen years later, Jensen et *al*., have prepared the compound by hydrothermal method and described an accurate structural model for the α-phase.[27] However nobody has described the crystal structures of the high temperature phases till date.

β-$Li_4Zn(PO_4)_2$ has been speculated to be isostructural to γ-Li_3PO_4,[25,27] which is well-known since long as a good Li^+ conductor.[21] More specifically, this compound can be viewed as Li_3PO_4 with two Li^+ substituted by one Zn^{2+}, and since there is no twofold positions in Li_3PO_4 to accommodate the extra Zn^{2+}, the Zn^{2+} and vacancies are probably disordered in fourfold Li sites. This could explain the higher conductivity reported for the β phase, bearing in mind that in solid electrolytes, disordered polymorphs possess greater conductivity than their ordered counterparts.[28–30] Hence, the high temperature disordered polymorphs are of great interest, with in particular a huge attention which is paid to the stabilization of such phases at room temperature. Various methods have been developed to stabilize the high temperature phase at room temperature, such as, quenching[31], nanostructuring[28,32], or varying synthesis condition like using certain precursors[22]. Nevertheless, the most effective method is the aliovalent substitution[21,33–35], which creates Li^+ deficiency and disorder in the Li-sublattice which eventually can lead to the stabilization of the disordered phase.

In this work, a similar strategy has been carried out and we found as described herein that the partial substitution of Zn^{2+} by trivalent Ga^{3+} in $Li_4Zn_{1-x}Ga_x(PO_4)_2$ (x = 0.5) can successfully stabilize the β-phase at room temperature. At lower substitution levels (x = 0.3), $Li_{3.7}Zn_{0.7}Ga_{0.3}(PO_4)_2$ crystallizes into an intermediate β' phase. The structure of the β and β'-phases were solved for the first time and we found that they are disordered polymorphs of the low temperature α-phase. Additionally, the β-phase shows a higher ionic conductivity along with reduced activation energy than the α-polymorph.

EXPERIMENTAL SECTION

Synthesis. Samples of $Li_4Zn(PO_4)_2$ and $Li_4Zn_{1-x}Ga_x(PO_4)_2$ were prepared by classical solid state syntheses. Stoichiometric amounts of Li_2CO_3 (Sigma Aldrich, 99%), ZnO (Sigma Aldrich, 99%), $NH_4H_2PO_4$ (Alfa Aesar, 98%) and Ga_2O_3 (Alfa Aesar, 99.99%) were used as precursors. They were mixed homogeneously by ball-milling for 20 mins with stainless-steel balls in a stainless-steel vial using SPEX-8000M mixer-miller and pressed into a pellet subsequently. The different pellets were heated in alumina boats for 36 hours at 800 °C after a ramp of 1 °C/min, followed by quenching in air. For the high-energy ball-milling synthesis of the β-$Li_4Zn(PO_4)_2$, the as-prepared α-$Li_4Zn(PO_4)_2$ sample was continuously milled for 2 hrs using balls-to-powder weight ratio of 40.

Characterization. Powder X-ray diffraction (XRD) patterns were recorded in Bragg–Brentano geometry with a Bruker D8 Advance diffractometer equipped with a Cu K_α radiation (λ_1 = 1.54056 Å, λ_2 = 1.54439 Å) and a LynxEye detector. Evolution of XRD patterns of the samples with temperature were monitored *in situ* in the same diffractometer equipped with an Anton Paar HTK 1200N furnace to control the temperature. A ramping rate of 2 °C/min was applied. Differential scanning calorimetry (DSC) measurements were done in air using a STA 449C Netzsch apparatus at a rate of 10 °C/min.

High-resolution neutron diffraction was performed on the HRPT instrument at SINQ-PSI (Villigen, Switzerland) with a wavelength λ = 1.494 Å. All patterns were refined using the Rietveld method[36] as implemented in the FullProf program[37]. Bond Valence Energy Landscape maps (BVEL) were generated according to the method developed by Adams,[38] using the program BondSTR as implemented in the FullProf Suite[37]. For the BVEL maps, calculations of Li conduction paths were done after the removal of pre-existing Li in the unit cell and also after removing Zn and Ga ions located at Li sites. Anionic neighbors up to 8 Å were considered.

Electrochemical Impedance Spectroscopy (EIS) was used to determine the Li-ion conductivity of the samples. The AC impedance measurements were made using a Bio-Logic MTZ-35 impedance analyzer equipped with a HTF-1100 furnace. To perform the measurements, pellets of ~8 mm diameter and ~1.5 mm thickness were obtained by cold-pressing using a uniaxial pressure of ~5 bars in a hydraulic press and were densified by sintering at 700 °C for 6 hours while heated and cooled at a rate of 1 °C/min. In one exception of low-temperature sintering, the pellet of ball-milled β-$Li_4Zn(PO_4)_2$ was sintered at 200 °C for 4 days. All the sintered pellets were found to have a similar density of 75-80% with respect to the crystallographic density of $Li_4Zn(PO_4)_2$ (2.88 g/cm^3), hence our reported conductivity values were not corrected by the pellet porosities.

The AC impedance measurements were performed using platinum (Pt) blocking electrodes, by applying a sinusoidal signal of 500 mV amplitude over a frequency range of 10 MHz to 1 Hz. A thin foil of carbon was placed between the Pt electrode and the pellet in order to improve the electrode contact. The measurements were carried out in the temperature range of 100–600 °C with an accuracy of ±1 °C and were soaked for 15 mins at each measurement temperature prior triggering each sweep of frequency dependent impedance measurement at the temperature.

RESULTS AND DISCUSSIONS

Structural characterization. X-ray and neutron powder diffraction were used to examine the crystal structures of $Li_4Zn(PO_4)_2$ in its low temperature α- and high temperature β- forms. The XRD pattern of the as-prepared pristine sample, α-$Li_4Zn(PO_4)_2$ (room temperature form), can be perfectly fitted with a monoclinic unit cell having a $P\ 2_1/c$ space group and lattice parameters a = 8.11990(16) Å, b = 10.24192(13) Å, c = 8.10549(15) Å, β = 104.8589(9)°, V = 651.538(2) Å^3, with Z = 4, using the structural model reported earlier[27]. The combined Rietveld refinement of the neutron and XRD patterns is shown in Figures 1a and 1b and the resulting structural parameters are reported in Table 1. The structure of α-$Li_4Zn(PO_4)_2$ is plotted in Figure 2. It consists of corner sharing ZnO_4 and PO_4 tetrahedra forming layers along the b-c plane, which are stacked along [100]. These layers are separated by Li atoms which are also in tetrahedral coordination.

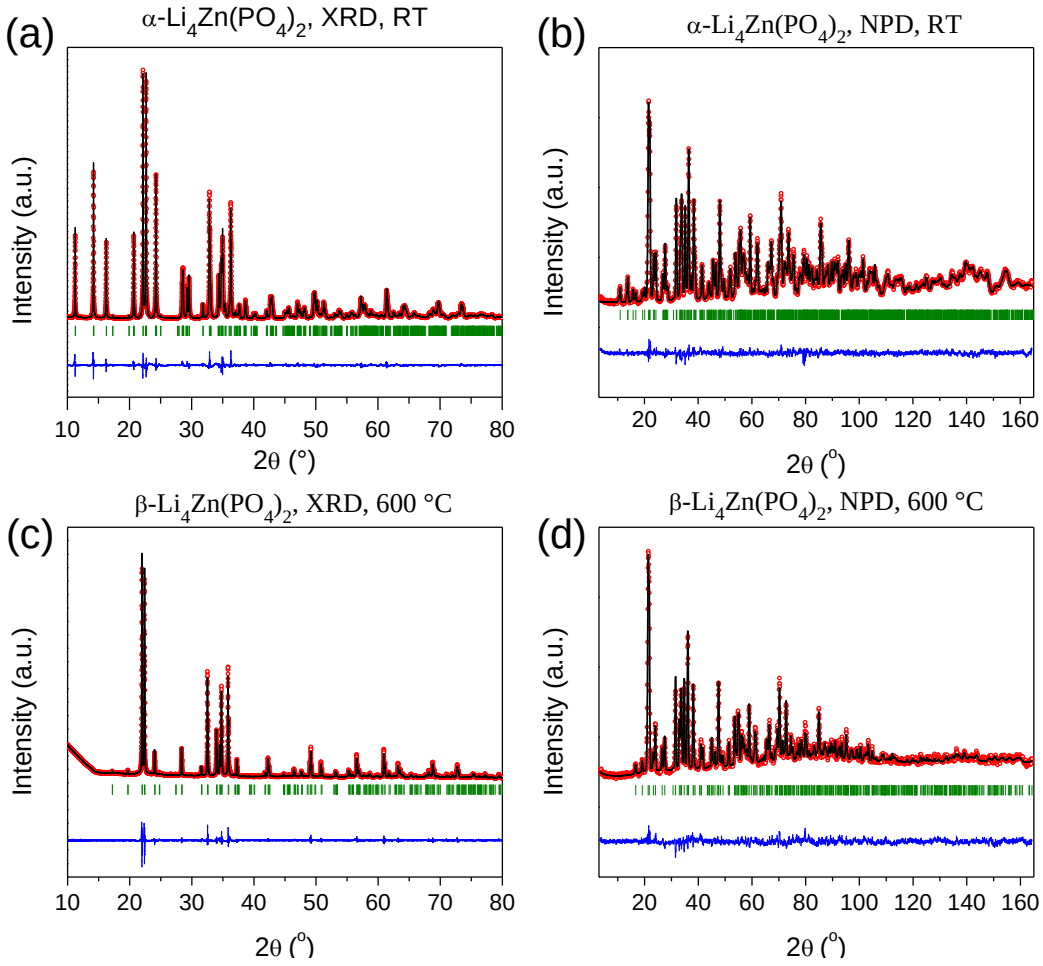

Figure 1. Rietveld refinement of the XRD and NPD patterns of α- and β-$Li_4Zn(PO_4)_2$, measured at room temperature (a, b) and at 600°C (c, d). The red circles, black continuous line, blue line and green tick bars represent the observed, calculated, and difference patterns, and Bragg positions, respectively.

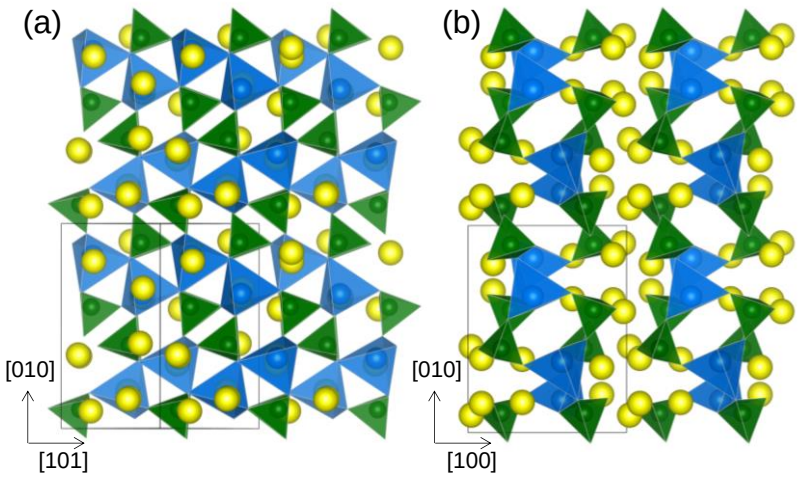

Figure 2. Crystal structure of $Li_4Zn(PO_4)_2$; (a) along $[\bar{1}01]$, (b) along [001]. Li is shown in yellow; ZnO_4 and PO_4 tetrahedra are colored in blue and green, respectively.

Table 1. Structural Parameters for α-$Li_4Zn(PO_4)_2$, deduced from the Rietveld refinement of the neutron pattern at room temperature. Isotropic temperature factors (B_{iso}) were constraint to be equal for a same chemical species.

α-$Li_4Zn(PO_4)_2$, room temperature Space group *P* $2_1/c$ *a* = 8.11990(16) Å, *b* = 10.24192(13) Å, *c* = 8.10549(15) Å, β = 104.8589(9)° *V* = 651.538(2) Å^3, *Z* = 4						
atom	site	x	y	z	B_{iso}	Occupancy
Zn1	4*e*	0 0.5938(8)	0.1567(7)	0.0933(8)	0.72(9)	1
P1	4*e*	0.2125(6)	0.4079(4)	0.4726(7)	0.30(4)	1
P2	4*e*	0.2706(7)	0.5916(4)	0.0353(7)	0.30(4)	1
O1	4*e*	0.1628(7)	0.1505(6)	0.1313(6)	0.535(17)	1
O2	4*e*	0.0620(7)	0.3992(4)	0.3115(7)	0.535(17)	1
O3	4*e*	0.3614(6)	0.3328(6)	0.4378(6)	0.535(17)	1
O4	4*e*	0.2518(6)	0.5549(4)	0.5046(6)	0.535(17)	1
O5	4*e*	0.1230(6)	0.6536(6)	0.0888(7)	0.535(17)	1
O6	4*e*	0.5688(6)	0.1017(4)	0.3127(7)	0.535(17)	1
O7	4*e*	0.6926(6)	0.3308(6)	0.1152(6)	0.535(17)	1
O8	4*e*	0.2249(6)	0.0465(4)	0.4769(6)	0.535(17)	1
Li1	4*e*	0.3484(20)	0.1466(17)	0.341(2)	0.39(10)	1
Li2	4*e*	0.1164(19)	0.3395(18)	0.1121(19)	0.39(10)	1
Li3	4*e*	0.0203(19)	0.0738(9)	0.269(2)	0.39(10)	1
Li4	4*e*	0.150(2)	0.8355(16)	0.157(2)	0.39(10)	1

The α-$Li_4Zn(PO_4)_2$ phase is known to undergo phase transition at high temperature to β-$Li_4Zn(PO_4)_2$,[27,26] but the crystal structure of β-$Li_4Zn(PO_4)_2$ was never reported, to our best knowledge. Hence we have carried out systematic investigations of the phase transition and finally have been able to deduce a structural model for the β-$Li_4Zn(PO_4)_2$ phase. Differential scanning calorimetry (DSC), shown in Figure 3a, of the as-prepared $Li_4Zn(PO_4)_2$ sample clearly depicts the α → β transitions at ca. 443 °C on heating, with an activation enthalpy of 11.7 kJ/mol (endothermic). On cooling, the DSC trace shows the reversible process with a thermal hysteresis of ∼15 °C indicating that the transition is of first order. This phase transition was monitored by temperature dependent XRD experiments and the diffractograms are gathered in Figure 3b. Upon heating, XRD patterns of α-$Li_4Zn(PO_4)_2$ show a small shift towards lower angles due to thermal expansion, until the temperature reaches 430°C. Above this temperature, the XRD pattern changes and looks similar to the one previously reported for the β form. On cooling, this process is reversible and the α-phase is recovered below 420°C, see Figure S1.

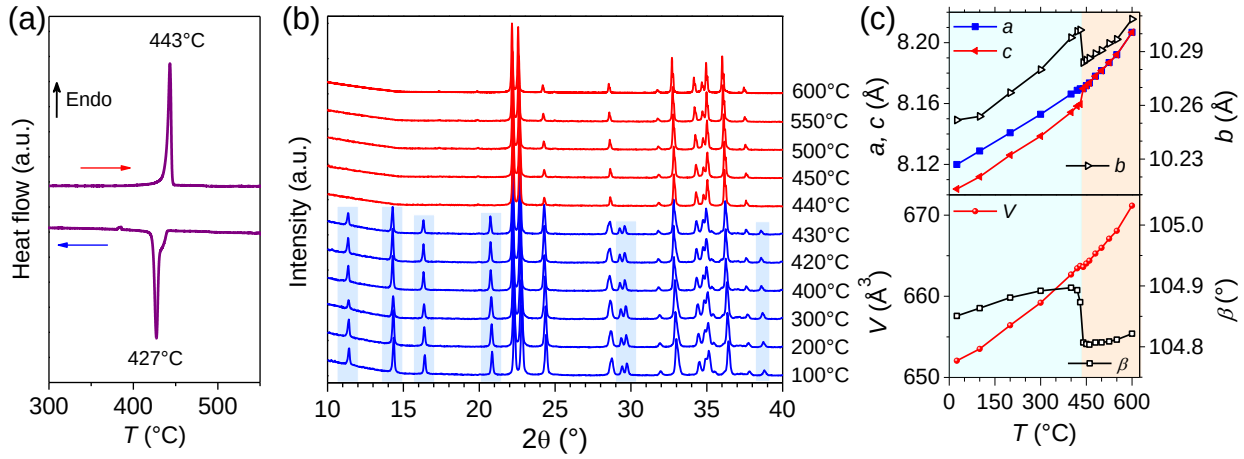

Figure 3. (a) DSC curve of $Li_4Zn(PO_4)_2$, measured in air with a heating and cooling rate of 10 °C/min. (b) Evolution of the XRD patterns of $Li_4Zn(PO_4)_2$ between 100 and 600 °C on heating. Values of temperatures corresponding to the patterns are indicated at the right. The patterns colored in blue and red corresponds to the α- and β- polymorphs, respectively, and the peaks that disappear for the β- phase has been indicated by blue backgrounds. (c) Evolution of lattice parameters with respect to temperature. The lattice parameters have been converted to monoclinic unit cell setting pertaining to the α- crystal structure for comparison. The blue and red regions correspond to the α- and β- phases, respectively.

Note that our efforts to quench the high temperature β phase at room temperature were unsuccessful; therefore we directly used the pattern recorded at 600°C to solve the structure for the β phase. The β phase presents a powder pattern similar to the α-phase, except for some peaks that have disappeared, especially in the low angle region. This relative similarity in diffraction pattern hints for a structural relationship between the α- and the β- structures. The XRD pattern of β-$Li_4Zn(PO_4)_2$ at 600°C could be indexed using the Dicvol program[36] with an orthorhombic unit cell with lattice parameters a = 10.30571(4) Å, b = 6.50156(3) Å and c = 5.00496(2) Å, leading to a unit cell volume V = 335.348(2) Å^3 that is half the volume of the room temperature monoclinic unit cell and therefore can accommodate two formulas per unit cell (Z = 2). The orthorhombic unit cell vectors are linked to the monoclinic α-$Li_4Zn(PO_4)_2$ ones by the following relation:

$$\begin{pmatrix} \mathbf{a}_{\text{ortho}} \\ \mathbf{b}_{\text{ortho}} \\ \mathbf{c}_{\text{ortho}} \end{pmatrix} = \begin{pmatrix} 0 & 1 & 0 \\ ½ & 0 & -½ \\ ½ & 0 & ½ \end{pmatrix} \begin{pmatrix} \mathbf{a}_{\text{mono}} \\ \mathbf{b}_{\text{mono}} \\ \mathbf{c}_{\text{mono}} \end{pmatrix}$$

Systematic extinctions were found to be consistent with *P n m a* space group. The orthorhombic unit cell is plotted on top of the α structure in Figure 4a, and where, looking at two adjacent orthorhombic unit cells, it clearly appears that the high temperature β phase should involve a disorder between Zn and Li2 atoms to comply invariance through lattice translation. Therefore the XRD and neutron diffraction patterns (NPD) of the β-phase recorded at 600°C were then simultaneously refined by the Rietveld method, introducing mixing between Zn and Li cations.

Table 2. Structural Parameters for β-$Li_4Zn(PO_4)_2$, deduced from the combined Rietveld refinement of the XRD and neutron patterns recorded at 600 °C. Isotropic temperature factors (B_{iso}) were constraint to be equal for a same chemical species.

β-$Li_4Zn(PO_4)_2$, high temperature form Space group *P n m a* *a* = 10.2974(4) Å, *b* = 6.5021(3) Å, *c* = 5.0011(2) Å, *V* = 334.85(2) Å^3, *Z* = 2						
atom	site	x	y	z	B_{iso}	Occupancy
P1	4*c*	0.40840(15)	3/4	0.8105(3)	1.87(7)	1
O1	8*d*	0.3415(2)	0.5553(3)	0.7009(5)	2.77(7)	1
O2	4*c*	0.5522(2)	3/4	0.7330(6)	2.55(9)	1
O4	4*c*	0.6039(3)	1/4	0.8808(5)	2.63(9)	1
Li1/Zn1	8*d*	0.1546(2)	0.4995(3)	0.8074(4)	3.10(8)	0.75/0.25
Li3	4*c*	0.9207(17)	1/4	0.780(4)	4.45(8)	0.5

The deduced structural model is shown in Figure 4b, the corresponding Rietveld refinements in Figures 1c and 1d and structural parameters are gathered in Table 2. Lastly, all temperature-dependent XRD patterns were Rietveld refined and the evolution of lattice parameters of the $Li_4Zn(PO_4)_2$ with temperature is summarized in Figure 3c using the monoclinic description for the β phase for an easier comparison. It can be noticed that the unit cell volume monotonously increases with T and exhibits a slight discontinuity at the transition, as expected from a first order phase transition. Moreover it should be noted that this volume increase results from anisotropic changes in the *b*, *c* and β unit cell parameters.

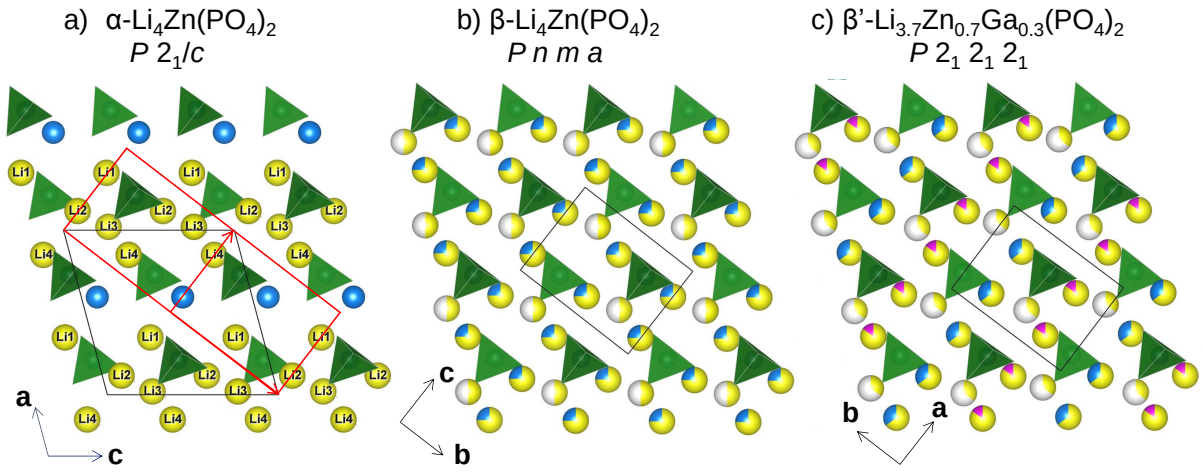

Figure 4. Crystal structure of (a) α-$Li_4Zn(PO_4)_2$, (b) β-$Li_4Zn(PO_4)_2$ and (c) β'-$Li_{3.7}Zn_{0.7}Ga_{0.3}(PO_4)_2$; in (a), the monoclinic α unit cell is plotted in black and the orthorhombic β cell is shown in red. For sake of clarity, only half of the unit cell content ($0 \le y \le ½$ in the monoclinic setting) is shown. Li, Zn and Ga are shown in blue, yellow and pink, respectively and PO_4 tetrahedra are colored in green.

Having found that the β-$Li_4Zn(PO_4)_2$ is a disordered counterpart of the α-$Li_4Zn(PO_4)_2$ polymorph, it became interesting to stabilize this phase at room temperature. Since ball-milling is known to increase disorder by repeated particles fracturing and welding, as was demonstrated recently for sulphates[39], we tried to stabilize the β phase by ball-milling. More specifically, the as-prepared α-$Li_4Zn(PO_4)_2$ was ball

milled for 2 hours. The XRD pattern of the obtained powder shows broad peaks that can be nicely fitted with the structural model of the β-$Li_4Zn(PO_4)_2$ polymorph deduced earlier (Figure S2). From the width of the Bragg peaks, we could further deduce that the ball-milled powder is made of particles with crystallites size of 10(±2) nm.

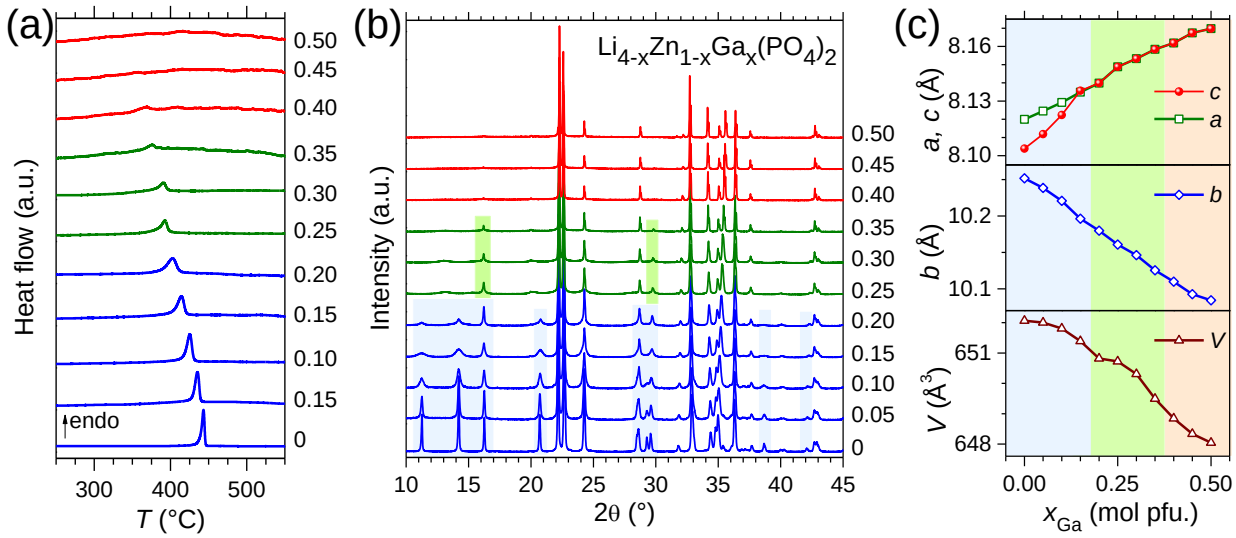

Figure 5. (a) DSC curves of $Li_{4-x}Zn_{1-x}Ga_x(PO_4)_2$ samples, measured in air with a heating and cooling rate of 10 °C/min. Values of x corresponding to the patterns are indicated at the right. (b) XRD patterns of $Li_{4-x}Zn_{1-x}Ga_x(PO_4)_2$ samples, measured at room temperature. Values of x corresponding to the patterns are indicated at the right. The patterns colored in blue, green and red corresponds to the α-, β'-, and β- polymorphs, respectively, and the peaks that disappear from the α- and β- phases have been indicated by blue and green backgrounds, respectively. (c) Evolution of lattice parameters with respect to Ga content. The lattice parameters have been converted to monoclinic unit cell setting for comparison. The blue, green, and red regions correspond to the α-, β'-, and β- phases, respectively.

Chemical substitution was then explored as an alternative to ball milling to introduce disorder. More precisely, we attempted the partial substitution of Zn^{2+} with M = Al^{3+}, Ga^{3+} and In^{3+} in $Li_4Zn(PO_4)_2$ with the hope to create disorder in Li-sublattice by introducing Li^+ deficiency for charge compensation and hence to promote the β-phase stabilization. All samples of nominal compositions of $Li_{4-x}Zn_{1-x}M_x(PO_4)_2$ were prepared by quenching the pellet from the synthesis temperature (800°C). We found that Al^{3+} and In^{3+} are unable to form solid solutions with $Li_4Zn(PO_4)_2$, leading to impurity phases consisting of $AlPO_4$ and not yet identified phase, respectively. This contrasts with the incorporation of Ga^{3+} that was successful for x ≤ 0.5 mol pfu., beyond which secondary phases were found to form. Figure 5b shows the room temperature XRD patterns of as-prepared $Li_{4-x}Zn_{1-x}Ga_x(PO_4)_2$ samples with 0 ≤ x ≤ 0.5. The Bragg peaks gradually shift towards higher 2θ angles, indicating that the unit cell volume decreases with insertion of Ga^{3+}, as expected from the smaller ionic radii of Ga^{3+} versus Zn^{2+} (Figure 5c). Moreover, low angle XRD peaks gradually broaden and their intensity decreases with increasing the Ga content, prior to finally disappear completely for 0.3 mol Ga pfu. Note that for x = 0.3 the collected XRD pattern appears similar, at first sight, to the one of the high temperature β-$Li_4Zn(PO_4)_2$ phase, hence suggesting that Ga-substitution is efficient to preserve some Li/Zn disorder even at room temperature. Taking a closer look

at the $Li_{3.7}Zn_{0.7}Ga_{0.3}(PO_4)_2$ pattern, it appears that all peaks can be indexed with the same orthorhombic cell as β-$Li_4Zn(PO_4)_2$ with slightly smaller lattice parameters, a = 4.9391(2) Å, b = 6.4803(3) Å, c = 10.1468(5) Å, and V = 324.77(3) Å^3. However the presence of (011) and (013) peaks, at 2θ values of 16.2° and 29.8°, respectively, rules out the *P n m a* space group, and suggests its *P* 2_1 2_1 2_1 subgroup. A structural model was therefore constructed and Rietveld refined against both neutron and XRD patterns, simultaneously. The best structural model (Figure 4c), as deduced by combined neutron and X-ray diffraction refinements (Figure 6), was obtained by mixing Li and Zn on one site, and Li and Ga on another site. This structure, whose structural parameters are gathered in Table 3 and which will be denoted as β'- hereafter, only differs from the β- structure by the fact that the 8*d* site in *P n m a* splits into two crystallographic sites of multiplicity 4, indicating that introducing Ga segregates Zn and Ga on two distinct positions in *P* 2_1 2_1 2_1, both of them being mixed with Li.

Table 3. Structural Parameters for β'-$Li_{3.7}Zn_{0.7}Ga_{0.3}(PO_4)_2$ deduced from the combined Rietveld refinement of the XRD and neutron patterns recorded at RT.

β'-$Li_{3.7}Zn_{0.7}Ga_{0.3}(PO_4)_2$, room temperature Space group *P* 2_1 2_1 2_1 *a* = 4.9391(2) Å, *b* = 6.4803(3) Å, *c* = 10.1468(5) Å, *V* = 324.77(3) Å^3, *Z* = 2						
atom	site	x	y	z	B_{iso}	Occupancy
P	4*a*	0.1879(4)	0.0077(6)	0.3419(2)	0.92(5)	1
O1	4*a*	0.3045(11)	0.1887(7)	0.4158(4)	1.23(3)	1
O2	4*a*	0.2705(6)	0.0131(8)	0.1959(2)	1.23(3)	1
O3	4*a*	0.7091(11)	0.2999(8)	0.0953(4)	1.23(3)	1
O4	4*a*	0.1229(5)	0.4896(8)	0.1434(3)	1.23(3)	1
Li1/Ga1	4*a*	0.1826(15)	0.246(16)	0.5784(5)	0.97(8)	0.85/0.15
Li2/Zn2	4*a*	0.3092(8)	0.2531(9)	0.1032(3)	0.97(8)	0.65/0.35
Li3	4*a*	0.231(6)	0.532(6)	0.822(3)	2.1(7)	0.35

Table 4. Structural Parameters for β-$Li_{3.5}Zn_{0.5}Ga_{0.5}(PO_4)_2$ deduced from the combined Rietveld refinement of the XRD and neutron patterns recorded at RT.

β-$Li_{3.5}Zn_{0.5}Ga_{0.5}(PO_4)_2$, room temperature Space group *P n m a* *a* = 10.08925(3) Å, *b* = 6.51080(2) Å, *c* = 4.935878(15) Å, *V* = 324.162(0.054) Å^3, *Z* = 2						
atom	site	x	y	z	B_{iso}	Occupancy
P1	4*c*	0.40726(18)	0.75	0.8106(4)	1.16(7)	1
O1	8*d*	0.3384(3)	0.5511(3)	0.6966(5)	1.89(5)	1
O2	4*c*	0.5531(3)	0.75	0.7319(7)	1.89(5)	1
O4	4*c*	0.6072(3)	0.25	0.8766(6)	1.89(5)	0.1
Li1/Zn1/Ga1	8d	0.1589(2)	0.5013(3)	0.8123(4)	1.37(8)	0.750/0.125/0.125
Li3	4c	0.940(3)	0.25	0.900(7)	1.37(8)	0.5

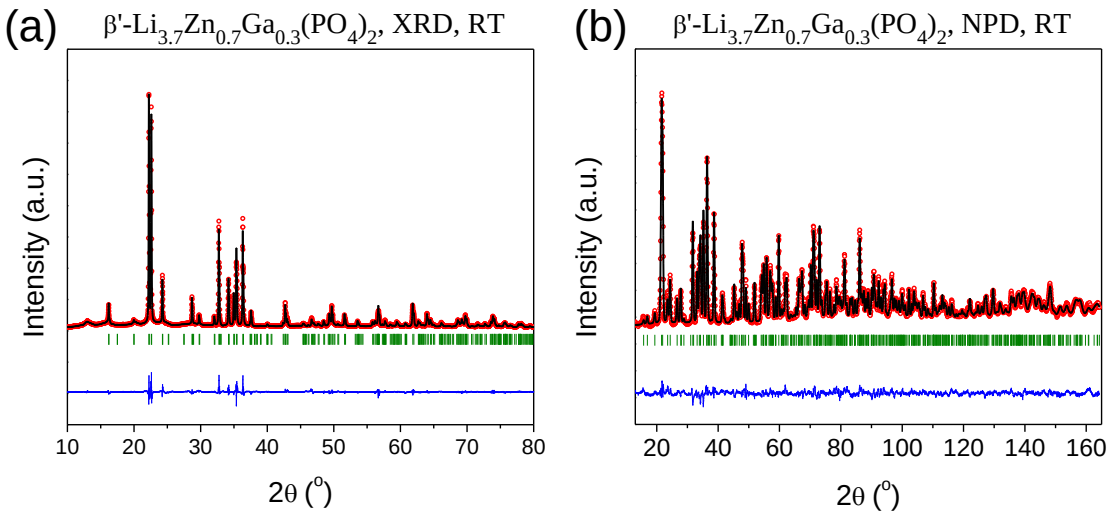

Figure 6. Rietveld refinement of (a) XRD, and (b) NPD patterns of β'-$Li_{3.7}Zn_{0.7}Ga_{0.3}(PO_4)_2$, measured at room temperature. The red circles, black continuous line, blue line and green tick bars represent the observed, calculated, and difference patterns, and Bragg positions, respectively.

Further substitution of Zn with Ga leads to disappearance of the (011) and (013) peaks in the XRD patterns, as evident from Figure 5b. This confirms the stabilization of the β-polymorph at room temperature with Ga concentration ≥0.35 mol pfu. The $Li_{3.5}Zn_{0.5}Ga_{0.5}(PO_4)_2$ compound produces a XRD pattern fully consistent with the *P n m a* space group involving a full Li/Zn/Ga disorder, as the high temperature pure Zn compound. In order to deduce a structural model for Ga-substituted β-phase, we performed a combined Rietveld refinement of the neutron and XRD patterns of $Li_{3.5}Zn_{0.5}Ga_{0.5}(PO_4)_2$ recorded at room temperature, as shown in Figure S3. The patterns could be fitted perfectly in *P n m a* space group with lattice parameters of *a* = 10.08917(3) Å, *b* = 6.51079(2) Å, *c* = 4.935843(16) Å, and *V* = 324.16(5) $Å^3$. The structural parameters are summarized in Table 4.

At this stage, it is worth reminding that all Ga-substituted samples mentioned previously were prepared by quenching from their synthesis temperature (800°C). Samples prepared by cooling slowly to room temperature (1 °C/min) and denoted as sc-$Li_{4-x}Zn_{1-x}Ga_x(PO_4)_2$ hereafter show slight but notable discrepancy in the XRD patterns compared to those prepared by quenching, for Ga contents of x = 0.3 and above. Two compounds, sc-$Li_{3.7}Zn_{0.7}Ga_{0.3}(PO_4)_2$ and sc-$Li_{3.5}Zn_{0.5}Ga_{0.5}(PO_4)$, were examined with special care. At room temperature, both samples present a XRD pattern characteristic of the β'- phase (*P* 2_1 2_1 2_1 (011) and (013) peaks at 2θ = 16.3° and 29.9°, highlighted in green) along with many additional small peaks indicated with stars in Figure 7a, 7b. To establish the origin of these additional peaks and to understand the relations with the quenched samples, we performed a temperature-dependent XRD study of the compositions mentioned above. Upon heating, the XRD pattern of the sc-$Li_{3.7}Zn_{0.7}Ga_{0.3}(PO_4)_2$ sample transforms into the β structure (*P n m a* space group) at 380°C, as indicated by the disappearance of all additional peaks and the (011) & (013) peaks of the β'- phase (Figure 7a). For the sc-$Li_{3.5}Zn_{0.5}Ga_{0.5}(PO_4)_2$ sample, the evolution of the XRD pattern is slightly more complex since we observe two successive transitions. The first one occurs at 380°C and corresponds to the disappearance of the β'-related peaks and most of the small peaks, indicating a transition to a β-like structure (Figure 7b). However, few tiny peaks (e.g. at 2θ = 13°) still persist above 380°C and disappear only at 750°C. At 800°C,

the pattern is fully alike the β one with all peaks being indexed in the *P n m a* space group. The tiny additional peaks shown for both slow-cooled compounds should therefore be considered as two separate sets of peaks, as they disappear at different temperatures for 0.5 Ga. The set that disappears at 380°C can be indexed with a propagation vector $\mathbf{k_1}$ = (0.37, 0.47, 0) related to the *P* 2_1 2_1 2_1 cell with lattice parameters *a* = 4.94 Å, *b* = 6.50 Å, and *c* = 10.11 Å. The second set of peaks, which disappears at higher temperature for Ga content of 0.5, can be indexed with $\mathbf{k_2}$ = (0, 0, 0.52). The corresponding Rietveld refinement of sc-$Li_{3.7}Zn_{0.7}Ga_{0.3}(PO_4)_2$ is shown in Figure S5. Therefore these additional peaks can be tentatively considered as superstructure peaks, arising from complex Li/Zn/Ga/vacancies ordering and/or Ga/Zn/Li chemical composition fluctuations. Further studies are needed to fully solve the underpinned complexity. Similarly, the quenched samples were examined by the temperature-dependent XRD experiments (Figures 7c,d). The β'-$Li_{3.7}Zn_{0.7}Ga_{0.3}(PO_4)_2$ sample was found to transform into the β- phase at 380 °C, as witnessed by the disappearance of the (011) and (013) peaks. This is fully confirmed by the combined refinement of the neutron and the XRD patterns recorded at 600°C. The results of the refinement with *P n m a* space group is presented in Figure S6, with structural parameters gathered in Table S1. Regarding the quenched β-$Li_{3.5}Zn_{0.5}Ga_{0.5}(PO_4)_2$, upon heating it transforms to the β' structure at 300 °C (therefore β'- should be the thermodynamically stable at room temperature) before transforming back to β at 340°C (Figure 7d). These experiments clearly indicate that quenching enables the stabilization of the high temperature phases at room temperature. Figure 8 summarizes the temperature-composition phase diagram we could establish from our experiments, for both the slow-cooled and quenched samples.

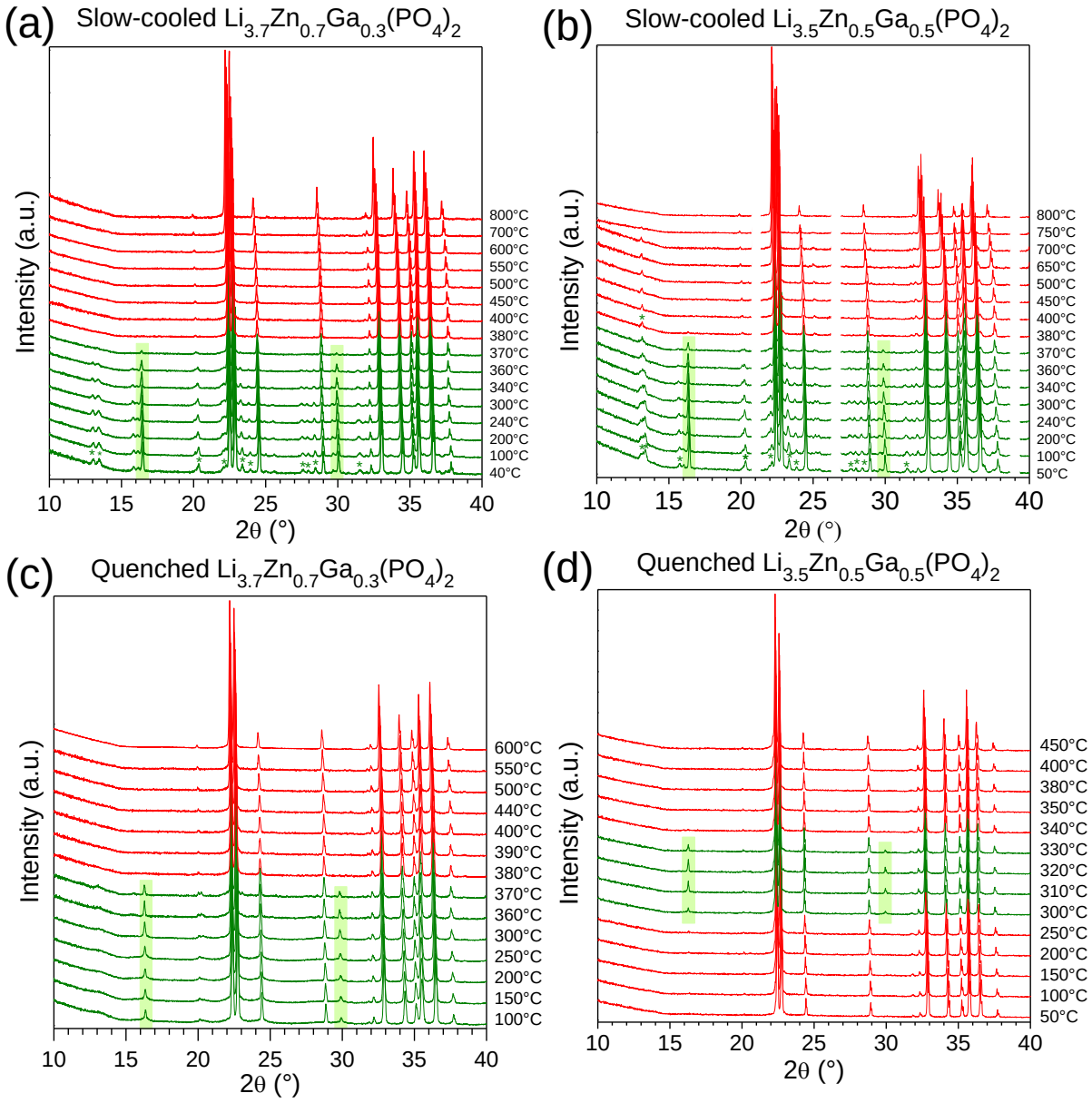

Figure 7. Evolution of XRD patterns of Ga-substituted samples: (a) sc-$Li_{3.7}Zn_{0.7}Ga_{0.3}(PO_4)_2$, (b) sc-$Li_{3.5}Zn_{0.5}Ga_{0.5}(PO_4)_2$, (c) quenched-$Li_{3.7}Zn_{0.7}Ga_{0.3}(PO_4)_2$ and (d) quenched-$Li_{3.5}Zn_{0.5}Ga_{0.5}(PO_4)_2$ with temperature. The patterns colored in green and red corresponds to the β'- and β- polymorphs, respectively, and the peaks that disappear for the β- phase has been indicated by green backgrounds.

Finally, to confirm the phase transitions with temperature in the quenched Ga-substituted samples, we measured the DSC curve of all quenched samples. The data have been summarized in Figure 5a and are in perfect agreement with high temperature XRD diffraction experiments. Transition temperatures deduced from DSC are reported as red stars in Figure 8. We see that the phase-transition temperatures to the high temperature β phase slightly decrease with increased Ga content, while the enthalpy of the phase transition reduces drastically and finally disappears for x_{Ga}= 0.45. This confirms that the substitution creates Li^+ deficiency and an inherently disordered Li-sublattice, which in turn

reduces the free energy associated with the ordering of Li-sublattice, eventually leading to stabilization of the disordered phase. Hence stabilization of the β-phase at room temperature can become possible by quenching.

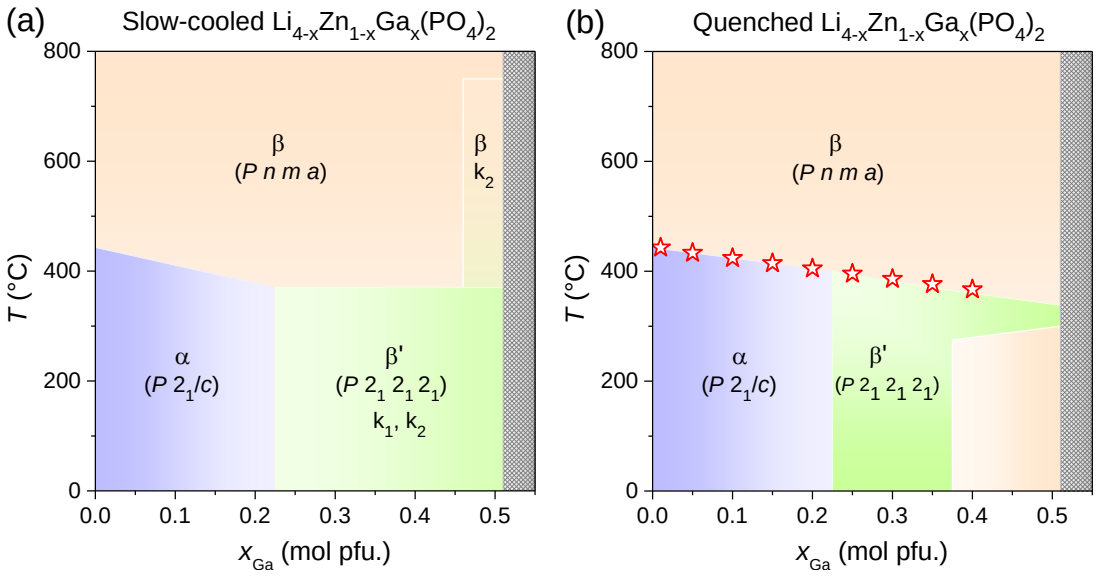

Figure 8. Temperature-Composition phase diagram of $Li_{4-x}Zn_{1-x}Ga_x(PO_4)_2$ compounds, deduced from temperature-dependent X-ray diffraction and DSC experiments (red stars). The black shaded region indicates the presence of secondary phases for Ga contents above 0.5 mol pfu.

Ionic Conductivity. We measured the ionic conductivity of all compounds by ac impedance spectroscopy over a broad frequency and temperature range. The impedance spectra were recorded on sintered pellets between ionically blocking platinum electrodes (see the experimental section for samples preparation). Figure 9a shows a typical Nyquist impedance plot of the sintered pellets of the pristine $Li_4Zn(PO_4)_2$ sample at 300 °C. Each recorded spectra shows a depressed semicircle at high frequencies followed by a Warburg tail at lower frequency region. The low frequency spike represents the impedance response due to the blocking of mobile Li ions at the electrode interface with Pt electrode and it confirms that the ac conductivity is ionic in nature. This was further confirmed by direct current (DC) polarization experiments, which indicates that the electronic contribution is negligible, see SI. The total ionic conductivity (σ_{tot}) was obtained by using the value of intercept of the Warburg tail with the semicircle. We have explored the impedance spectra further by examining the depressed semicircle at high frequency. The depression of the semicircle cannot be accounted by the inhomogeneities at the sample-electrode interface, hence the need of deconvolution of the semicircle to separate the different contributions. Since the impedance response of polycrystalline materials is expected to be composed of grain (bulk) and grain boundaries (surface) contributions, we decouple the semicircle to two contributions by fitting the whole impedance spectra to an equivalent circuit model $(R_g//Q_g)(R_{gb}//Q_{gb})W_o$ (inset of Figure 9a); where R and Q represent the resistance and constant phase element associated with the grains (*g*) or grain boundaries (*gb*) of the sample, respectively, and W_o is the Warburg resistance. The fitting produces an capacitances of ~10^{-12} F and ~10^{-11} F associated with the constant phase element, for the high and low frequency deconvoluted semicircles, respectively and hence can be assigned to grains

(σ_g) and grain boundaries (σ_{gb}) contributions, respectively[40]. A typical fitting is shown in Figure 9a. This assignment was further confirmed by calculating the characteristic resonance frequencies (f_r) of the semicircles which generally appear at the apexes of the deconvoluted semicircles; as indicated in Figure 9a. However, with increasing temperature, both grains and grain boundary responses gradually shift towards higher frequencies and finally move beyond the measurable frequency window of the instrument leaving only the Warburg tail observable. Hence deconvolution of grain conductivity (σ_g) and grain boundary conductivity (σ_{gb}) was not possible above ~300-400 °C for the samples and only σ_{tot} was obtained.

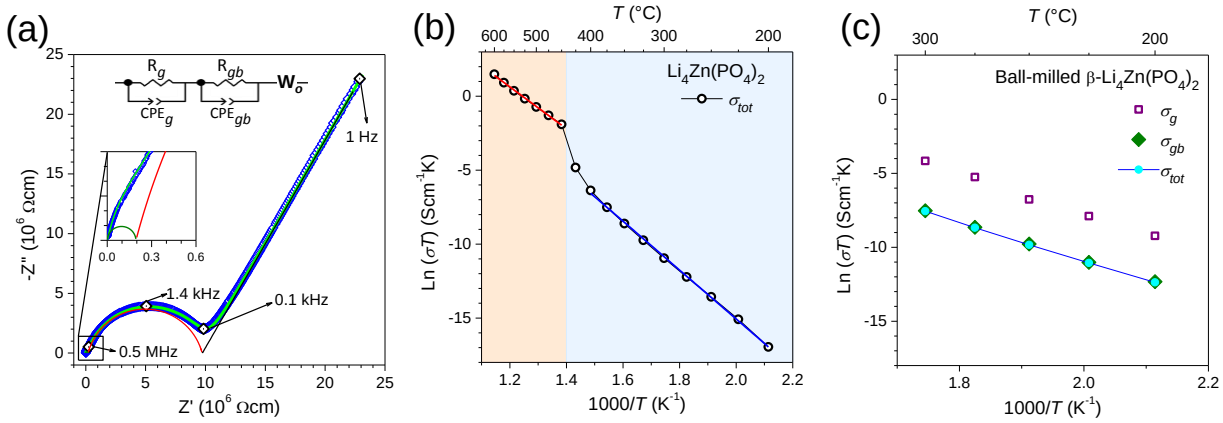

Figure 9. (a) Representative AC impedance spectra of $Li_4Zn(PO_4)_2$ sample recorded at 300 °C, the fitting has been shown by light green line on the curve. The deconvolution to different contributions, as obtained from the fitting, has been shown in the same curve and also zoomed in the inset. Contributions from the grains and grain boundary, has been indicated by green and red semicircles, respectively, and Warburg tail by black line. Some typical frequencies has also been indicated, the highest two of them are the resonance frequencies corresponding to grains and grain boundaries, respectively. Inset shows the equivalent circuit used to fit the spectra. Arrhenius plot of σ_{tot} of $Li_4Zn(PO_4)_2$ (b) and ball-milled β-$Li_4Zn(PO_4)_2$ (c); in (b) the blue and red background refers to α- and β- $Li_4Zn(PO_4)_2$ polymorph, respectively.

The variations of the ionic conductivity for the pristine $Li_4Zn(PO_4)_2$ over the temperature range of 200 - 375 °C are shown in Figure S7A and in Figure 10. There is a linear variation for the ln(σT) with temperature, indicative of a thermally activated Arrhenius type behavior $\sigma(T)=A/T\cdot\exp(-E_a/k_BT)$, where k_B is the Boltzmann constant, A is a pre-exponential factor and T is temperature). The room temperature $\sigma_{b,}$ $\sigma_{gb,}$ and σ_{tot} values of ~5.5×10^{-18}, ~3.5×10^{-19}, and ~1.8×10^{-19} S·cm^{-1}, respectively, were deduced by linear extrapolation of the Arrhenius plot to the room temperature, with a similar E_a of ~1.3 eV for all the conduction processes. Altogether, this implies that this compound is not a good conducting material at low temperature, at least in its α-form.

We next measured the conductivity of the pristine $Li_4Zn(PO_4)_2$ sample over a broader temperature range of 200 - 600 °C and reported the measured σ_{tot} values in Figure 9b. A sudden change in the slope of the Arrhenius plot occurs at ~425 °C; temperature at which the α→β structural transition was shown to occur. Note that the high temperature β-$Li_4Zn(PO_4)_2$ polymorph shows a much higher conductivity with an E_a of 1.1 eV and a room temperature σ_{tot} of 1.8×10^{-15} S·cm^{-1}. For sake of completion we also measured the transport properties of our new room temperature β-$Li_4Zn(PO_4)_2$ phase obtained by ball-milling of the α-$Li_4Zn(PO_4)_2$ phase (Figure 9c). Interestingly, the ball-milled β- sample shows an extrapolated RT σ_{tot} value of 2.4×10^{-15} S·cm^{-1}, nearly similar to that obtained from the high-temperature

β-phase of $Li_4Zn(PO_4)_2$ with however a slightly lower activation energy (Ea = 1.0 eV). We exploited this data further by decoupling the grains and grain boundaries contributions and found activations energies of 1.1 and 1.0 eV, respectively, with corresponding room temperature conductivities of $1.7x10^{-14}$ $S{\cdot}cm^{-1}$ (σ_g) and $3x10^{-15}$ $S{\cdot}cm^{-1}$ (σ_{gb}). Overall, this further confirms the better transport properties of the β-polymorph even when prepared at room temperature.

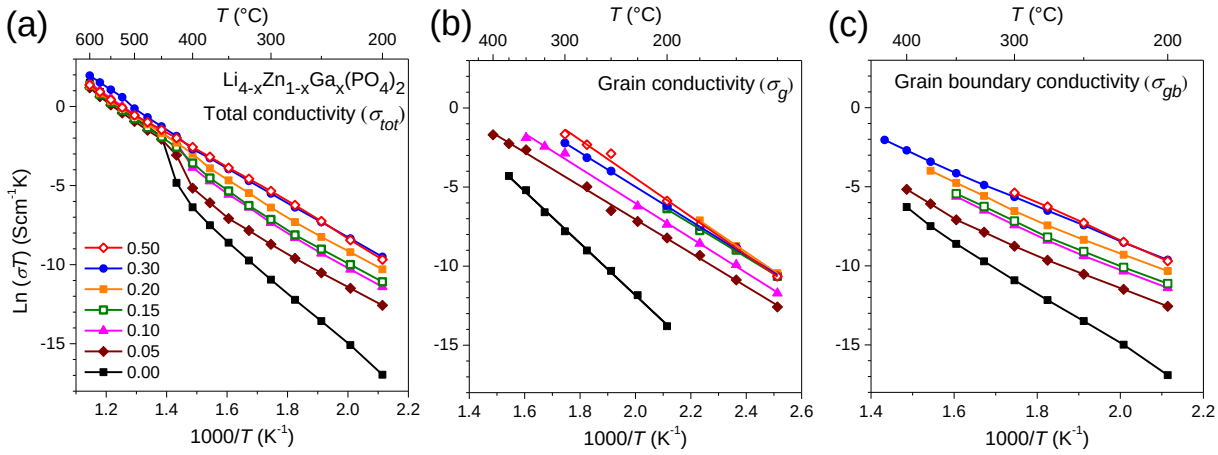

Figure 10. Arrhenius plot ionic conductivity showing σ_{tot} (a), σ_g (b) and σ_{gb} (c) of $Li_{4-x}Zn_{1-x}Ga_x(PO_4)_2$. Values of x are indicated in (a).

Encouraged by these findings, we also explored the transport properties of the quenched $Li_{4-x}Zn_{1-x}Ga_x(PO_4)_2$ samples. The results, shown in Figure 10, reveal a steady increase of the ionic conductivities together with a progressive smearing of the jump in conductivity at the α→β'/β transition with increasing the Ga^{3+} substitution (x_{Ga}). More specifically, the change of slope in conductivity at the structural transition gradually decreases till a Ga^{3+} content of 0.15 pfu. and then disappears completely with further increase of Ga content. This is consistent with the results obtained from XRD experiments which show that the β'-phase is formed beyond x_{Ga} =0.25 and also from DSC measurements which indicate a shift/smearing of the phase transition with increasing x_{Ga} content.

Table 5. Ionic conductivities of the $Li_{4-x}Zn_{1-x}Ga_x(PO_4)_2$ samples at RT obtained by extrapolation of the Arrhenius plot and at 200 °C and their activation energies (E_a). The blue, green and red background indicates α-, β'-, and β- phases, respectively.

x_{Ga}		σ_g (S·cm^{-1})			σ_{gb} (S·cm^{-1})			σ_{tot} (S·cm^{-1})		
		RT	200 °C	E_a (eV)	RT	200 °C	E_a (eV)	RT	200 °C	E_a (eV)
α-	0	$5.55\cdot10^{-18}$	$2.14\cdot10^{-9}$	1.32	$3.49\cdot10^{-19}$	$9.54\cdot10^{-11}$	1.30	$3.61\cdot10^{-19}$	$9.14\cdot10^{-11}$	1.3
	0.05	$1.44\cdot10^{-12}$	$5.7\cdot10^{-7}$	0.87	$4.23\cdot10^{-14}$	$7.42\cdot10^{-9}$	0.82	$4.10\cdot10^{-14}$	$7.33\cdot10^{-9}$	0.82
	0.1	$1.86\cdot10^{-12}$	$1.34\cdot10^{-6}$	0.92	$8.3\cdot10^{-14}$	$2.38\cdot10^{-8}$	0.85	$8.10\cdot10^{-14}$	$2.34\cdot10^{-8}$	0.85
	0.15	$6.46\cdot10^{-12}$	$3.63\cdot10^{-6}$	0.89	$2.65\cdot10^{-13}$	$3.13\cdot10^{-8}$	0.79	$1.75\cdot10^{-13}$	$3.10\cdot10^{-8}$	0.82
	0.2	$5.16\cdot10^{-12}$	$1.93\cdot10^{-6}$	0.95	$3.46\cdot10^{-13}$	$6.93\cdot10^{-8}$	0.82	$3.39\cdot10^{-13}$	$6.69\cdot10^{-8}$	0.83
β'	0.25	$6.0\cdot10^{-12}$	$5.93\cdot10^{-6}$	0.93	$4.88\cdot10^{-13}$	$1.13\cdot10^{-7}$	0.84	$4.54\cdot10^{-13}$	$1.11\cdot10^{-7}$	0.84
	0.3	$5.65\cdot10^{-12}$	$4.27\cdot10^{-6}$	0.91	$3.93\cdot10^{-13}$	$1.40\cdot10^{-7}$	0.86	$3.57\cdot10^{-13}$	$1.35\cdot10^{-7}$	0.87
β	0.4	$5.55\cdot10^{-12}$	$9.18\cdot10^{-6}$	0.95	$2.07\cdot10^{-13}$	$8.67\cdot10^{-8}$	0.88	$2.37\cdot10^{-13}$	$8.59\cdot10^{-8}$	0.87
	0.5	$1.63\cdot10^{-12}$	$5.94\cdot10^{-6}$	1.02	$1.41\cdot10^{-13}$	$1.30\cdot10^{-7}$	0.93	$1.30\cdot10^{-13}$	$1.27\cdot10^{-7}$	0.93

Further insight onto these transport properties of members of the $Li_{4-x}Zn_{1-x}Ga_x(PO_4)_2$ series can be gained by further analyzing the impedance data with the key values reported in Table 5. Firstly, there is an increase by several orders of magnitude of the σ_g room temperature values with increasing the x_{Ga} content so that σ_g of ~1– 2 x10^{-12} S·cm^{-1} can be obtained for x_{Ga} = 0.05, and 0.10 as compared to σ_g = $5.55\cdot10^{-18}$ S·cm^{-1} for x_{Ga}=0, while structure-wise the samples are still pertaining to the α-phase in the composition range. Such an effect is most likely nested in the increasing amount of disorder that we can spot by XRD from the broadening of Bragg reflections characterizing the α-polymorph (Fig 5b). Moreover, we notice a drastic fall in the E_a to 0.8 and 0.9 eV, respectively for the above mentioned compositions. Interestingly, we could observe that σ_{gb} tracks σ_g and increases to ~4-8 x10^{-14} S·cm^{-1} at RT, with σ_{tot} reaching ~4-8 x10^{-14} S·cm^{-1} at RT. Upon further increasing the x_{Ga} content beyond 0.05, the room temperature σ_g values slightly increase prior to saturate at values of ~6 x10^{-12} S·cm^{-1} (β-phase, Table 5) while structure-wise the compounds evolve from the α–phase to the β'-phase. Similarly σ_{gb} follows the same variation over this composition range while the activation energy remains nearly constant. It is only for samples having higher Ga contents (x_{Ga} > 0.40) and crystalizing in the β-structure that we observe a noticeable decease in σ_g to ~2 x10^{-12} S·cm^{-1} and an increase in E_a from 0.9 to 1.0 eV. Altogether, these findings fail to establish a direct correlation between structure and conductivity and further analysis is required to interpret this trend.

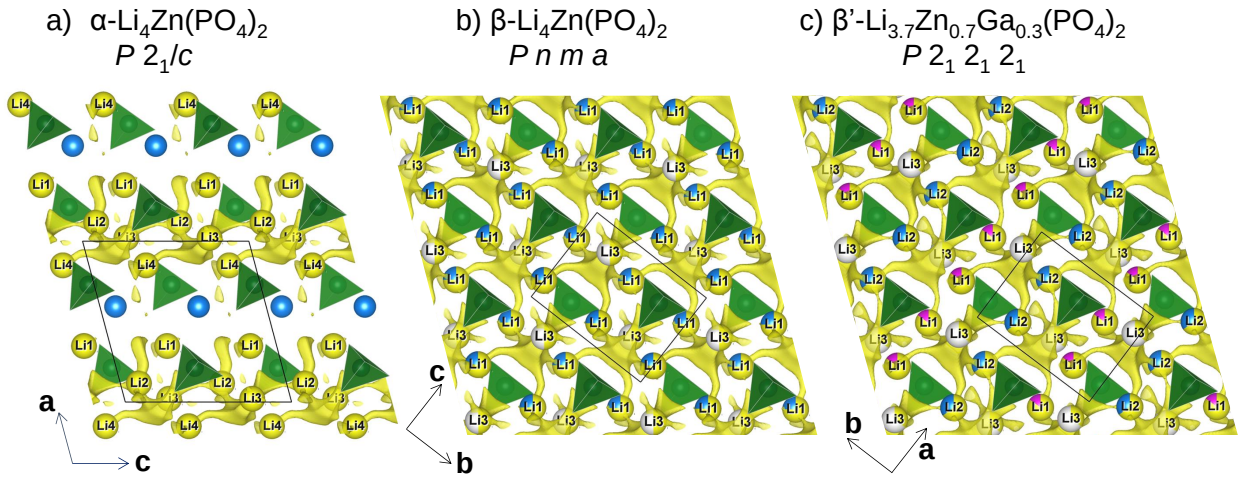

Figure 11. BVEL of (a) α-$Li_4Zn(PO_4)_2$, (b) high temperature β-$Li_4Zn(PO_4)_2$ and (c) β'-$Li_{3.7}Zn_{0.7}Ga_{0.3}(PO_4)_2$ at the percolation energies. The yellow domains indicates the migration paths for Li^+ in the structure, obtained using an iso-surface value of 1.05, 0.7, and 0.9 eV above the minimum energy, respectively. For color codes refer to Figure 4.

To retrieve qualitative information concerning the connection existing between structure and conductivity, BVEL was employed. The BVEL maps representing the Li^+ conduction pathways in the $Li_{4-x}Zn_{1-x}Ga_x(PO_4)_2$ polymorphs are shown in Figure 11. For α-$Li_4Zn(PO_4)_2$, infinite 2-D Li^+ percolation paths, involving Li2, Li3 and Li4 sites and not the sterically hindered Li1 site, appear along the b-c plane at 1.05 eV above the minimum energy. This is fully consistent with its layered crystal structure and Li^+ percolation occurs along the layers, whereas hopping of Li^+ between layers is not possible because of the Zn hindrance between the Li layers. This explains the high E_a and very low σ_g of the sample.

For the high temperature β-$Li_4Zn(PO_4)_2$ and β'-$Li_{3.7}Zn_{0.7}Ga_{0.3}(PO_4)_2$ phases, BVEL maps indicate a 3-D Li^+ percolation at 0.7 and 0.9 eV above the minimum energy, respectively. This comes in no surprise, because, in β- and β'-phases, the mixing between Li and Zn/Ga atoms on the same crystallographic positions breaks the layered nature of the α-polymorph, for which Li atoms are confined in the b-c planes. Thus in the β- and β'-polymorphs, Li ions can hop from sites to sites three-dimensionally. This is consistent with the lower E_a in the β- and β'- sample compared to the α-phase. Moreover, in β'/β-structures that present the same $(PO_4)^{3-}$ framework, Li3 is the only Li site not being mixed with Zn or Ga which accommodates the vacancies resulting from the charge compensation, (Figure 11), and BVEL maps indicate that ionic conduction takes place preferentially through this site. Therefore, this explains the little changes in σ_g values when the structure changes from β' to β-$Li_{3.5}Zn_{0.5}Ga_{0.5}(PO_4)_2$.

Although BVEL could account for the greater conductivity for the β'/β-polymorph as opposed to the α-one, the feasibility to obtain ionic conductivities for the α-polymorph as high as the β-phase at low Ga substitution level is not well understood. First let's recall that ionic conductivity is the result of a delicate balance between vacancies, disorder, and defects among others[17]. Numerous ionic conductors show order-disorder phase transition with the high temperature phase having usually a higher ionic conductivity, owing to its higher structural symmetry which flattens the potential landscape hence leading to reduced activation barrier for Li^+ jump as well as to its enhanced disorder that increases the number of energy equivalent Li-sites having partial occupancies.[41] The Ga-substitutions, besides

promoting structural disorder in the samples, introduces Li vacancies. However, the role of the vacancies remains questionable for the above observation as the ionic conductivity is nearly similar for α-$Li_{3.9}Zn_{0.9}Ga_{0.1}(PO_4)_2$ and β'-$Li_{3.9}Zn_{0.9}Ga_{0.1}(PO_4)_2$. To understand the respective contributions of vacancies and disorder, we plotted the variation of the $\log(\sigma_g)$ as a function of the concentration of Li vacancies and of the broadening of the Bragg peaks characteristic to the α-polymorph as an estimation of disorder in the samples, see Figure S7b. Note that the ionic conductivity drastically increases with increasing the amount of vacancies (x = 0.05) with afterwards another increase from x = 0.15 which seems to be related to an increase in structural disorder. We thus believe that the disorder, as evidenced from the peak broadening which indicates the presence of antiphase boundaries and/or small disordered β'/β domains in the structure, as was also observed in rocksalt-type oxides,[42] could trigger β'/β-like conduction even at low Ga-substitution level.

Additionally, the conductivity of a sample depends upon the surface contact of a grain with its neighbors, hence stressing the importance of grain boundaries vs. grain. Although ionic conductivity measurements are often reported as total conductivity (σ_{tot}) omitting grain (σ_g) and grain boundary values (σ_{gb}). Nevertheless, a simultaneous increase of (σ_b) and (σ_{gb}) with increasing the doping content is frequently reported was reported[43,44]. Our samples, being synthesized and sintered identically, are expected to have similar grain size and surface contacts. Thus for compounds having the highest conducting grains, the number of charge carriers crossing the grain boundaries will be greater as well, hence providing a possible explanation to the systematic tracking of grain and grain boundary conductivities observed in our samples.

CONCLUSIONS

In summary, we have explored in great details the rich crystal chemistry of $Li_4Zn(PO_4)_2$ and described how we could improve its ionic conductivity. We showed that this compound undergoes an order-disorder phase transition at ~443 °C, accompanied by a jump in its ionic conductivity. We solved the crystal structure of the high temperature orthorhombic β-polymorph, which appears to be derived from the low temperature monoclinic α-structure by preserving the PO_4^{3-} backbone, but presenting a disordered Li/Zn sublattice. The β-polymorph was found to have a higher conductivity than the α-phase.

We have demonstrated the feasibility to stabilize the β-polymorph at room temperature either by ball-milling the α phase, or by partial substitution of Zn^{2+} by Ga^{3+} in $Li_4Zn(PO_4)_2$. With 0.5 mol pfu Ga, we could successfully stabilize the pure β-polymorph at room temperature. The evolution of crystal structure from α-$Li_4Zn(PO_4)_2$ to β-$Li_{3.5}Zn_{0.5}Ga_{0.5}(PO_4)_2$ through an intermediate β'-$Li_{3.3}Zn_{0.7}Ga_{0.3}(PO_4)_2$ phase has been thoroughly characterized. The XRD pattern of $Li_{3.5}Zn_{0.5}Ga_{0.5}(PO_4)_2$, recorded at RT, could be refined with the structural model deduced for β-$Li_4Zn(PO_4)_2$ phase, with the Zn and Ga ions fully mixed in a disordered Li-sublattice. The β-$Li_{4-x}Zn_{1-x}Ga_x(PO_4)_2$ samples exhibit ionic conductivities of ~2-5 $x10^{-13}$ $S{\cdot}cm^{-1}$ at RT, by several orders of magnitudes higher than α-$Li_4Zn(PO_4)_2$. The higher crystal symmetry of the disordered β-$Li_4Zn(PO_4)_2$ enables to switch the conduction mechanism from 2-D to 3-D, thus rationalizes its higher conductivity.

Despite such a rich chemistry of $Li_4Zn(PO_4)_2$ and its Ga substitutes, needless to mention that this level of ionic conductivity is still far from desired performance to consider for practical applications. However, this report illustrates the role of disorder to ionic conduction and demonstrates how to use chemical substitutions to trigger room temperature stabilization of high temperature disordered-polymorphs. We hope that these insights will further boost the search of disordered compounds as new ionic conductors beyond the limited library of existing ionic conductors, keeping in mind their limitations to practical implications.

ASSOCIATED CONTENT

Supporting Information

The Supporting Information is available free of charge on the ACS Publications website:

DC Polarization measurement method; Evolution of XRD patterns of $Li_4Zn(PO_4)_2$ with temperature during cooling; Rietveld refinement of the XRD pattern of the ball-milled β-$Li_4Zn(PO_4)_2$ sample, measured at RT; Rietveld refinement of the XRD, and NPD patterns of β-$Li_{3.5}Zn_{0.5}Ga_{0.5}(PO_4)_2$ at RT; Crystal structure of β-$Li_{3.5}Zn_{0.5}Ga_{0.5}(PO_4)_2$, Rietveld refinement of the XRD pattern of sc-$Li_{3.7}Zn_{075}Ga_{0.3}(PO_4)_2$ at RT using the *P* 2_1 2_1 2_1 unit cell and $\mathbf{k_1}$ and $\mathbf{k_2}$ propagation vectors; Rietveld refinement of the XRD, and NPD patterns of β'-$Li_{3.7}Zn_{0.7}Ga_{0.3}(PO_4)_2$ at 600 °C; Structural Parameters for β'-$Li_{3.7}Zn_{0.7}Ga_{0.3}(PO_4)_2$ at 600 °C; Ionic conductivity of α-$Li_4Zn(PO_4)_2$; BVEL of β-$Li_{3.5}Zn_{0.5}Ga_{0.5}(PO_4)_2$ at the percolation energies; DC polarization plot and Arrhenius plot of DC conductivity of the β'-$Li_{3.7}Zn_{0.7}Ga_{0.3}(PO_4)_2$ (PDF)

Crystallographic data for α-$Li_4Zn(PO_4)_2$, RT (CIF)

Crystallographic data for β-$Li_4Zn(PO_4)_2$, 600°C (CIF)

Crystallographic data for β'-$Li_{3.7}Zn_{0.7}Ga_{0.3}(PO_4)_2$, RT (CIF)

Crystallographic data for β-$Li_{3.7}Zn_{0.7}Ga_{0.3}(PO_4)_2$, 600°C (CIF)

Crystallographic data for β-$Li_{3.5}Zn_{0.5}Ga_{0.5}(PO_4)_2$, RT (CIF)

AUTHOR INFORMATION

Corresponding Author

*E-mail: jean-marie.tarascon@college-de-france.fr.

Notes

The authors declare no competing financial interest.

ACKNOWLEDGMENTS

The authors thank Alexis Grimaud for fruitful discussions and for a careful reading of the manuscript, and Virginie Viallet for fruitful discussions. Vladimir Pumjakushin is acknowledged for his help on neutron diffraction experiments on HRPT at SINQ. S.S. thanks the Réseau sur le Stockage Electrochimique de l'Energie (RS2E) for funding of Ph.D.

REFERENCES

(1) Goodenough, J. B.; Kim, Y. Challenges for Rechargeable Li Batteries. *Chem. Mater.* **2010**, *22*, 587–603.

(2) Zeier, W. G.; Janek, J. A Solid Future for Battery Development. *Nat. Energy* **2016**, *1*, 16141.

(3) Larcher, D.; Tarascon, J.-M. Towards Greener and More Sustainable Batteries for Electrical Energy Storage. *Nat. Chem.* **2015**, *7*, 19–29.

(4) Goodenough, J. B.; Park, K. S. The Li-Ion Rechargeable Battery: A Perspective. *J. Am. Chem. Soc.* **2013**, *135*, 1167–1176.

(5) Gallagher, S. Boeing's Dreamliner Batteries "Inherently Unsafe"—And Yours May Be Too, https://arstechnica.com/information-technology/2013/01/boeings-Dreamliner-Batteries-Inherently-Unsafe-and-Yours-May-Be-Too/, (Accessed July 29, 2017). *Ars Tech* **2013**.

(6) Meier, F.; Woodyard, C. Feds Review Third Tesla Fire as Shares Fall Again, https://www.usatoday.com/story/money/cars/2013/11/07/third-Fire-in-Tesla-Model-S-reported/3465717/ (Accessed July 29, 2017). *USA Today* **2016**.

(7) Wang, L.; Wang, Y.; Xia, Y. A High Performance Lithium-Ion Sulfur Battery Based on a Li_2S Cathode Using a Dual-Phase Electrolyte. *Energy Environ. Sci.* **2015**, *8*, 1551–1558.

(8) Takemoto, K.; Yamada, H. Development of Rechargeable Lithium-Bromine Batteries with Lithium Ion Conducting Solid Electrolyte. *J. Power Sources* **2015**, *281*, 334–340.

(9) Huiqiao, L.; Yonggang, W.; Haitao, N.; Haimei, L.; Haoshen, Z. Rechargeable Ni-Li Battery Integrated Aqueous/nonaqueous System. *J. Am. Chem. Soc.* **2009**, *131*, 15098–15099.

(10) Faraday, M. Experimental Researches in Electricity, Third Series. *Philos. Trans. R. Soc. London* **1833**, *123*, 23–54.

(11) Hong, H. Y. P. Crystal Structure and Ionic Conductivity of $Li_{14}Zn(GeO_4)_4$ and Other New Li^+ Superionic Conductors. *Mater. Res. Bull.* **1978**, *13*, 117–124.

(12) J. Goodenough, H. P. H. and J. K. Fast Na^+-Ion Transport in Skeleton Structures. *Mater. Res. Bull.* **1976**, *11*, 203–220.

(13) Tachez, M.; Malugani, J. P.; Mercier, R.; Robert, G. Ionic Conductivity of and Phase Transition in Lithium Thiophosphate Li_3PS_4. *Solid State Ionics* **1984**, *14*, 181–185.

(14) Bates, J. B.; Dudney, N. J.; Gruzalski, G. R.; Zuhr, R. A.; Choudhury, A.; Luck, C. F.; Robertson, J. D. Electrical Properties of Amorphous Lithium Electrolyte Thin Films. *Solid State Ionics* **1992**, *53–56*, 647–654.

(15) Murugan, R.; Thangadurai, V.; Weppner, W. Fast Lithium Ion Conduction in Garnet-Type $Li_7La_3Zr_2O_{12}$. *Angew. Chem., Int. Ed.* **2007**, *46*, 7778–7781.

(16) Harada, Y.; Ishigaki, T.; Kawai, H.; Kuwano, J. Lithium Ion Conductivity of Polycrystalline Perovskite $La_{0.67-x}Li_{3x}TiO_3$ with Ordered and Disordered Arrangements of the A-Site Ions. *Solid State Ionics* **1998**, *108*, 407–413.

(17) Bachman, J. C.; Muy, S.; Grimaud, A.; Chang, H. H.; Pour, N.; Lux, S. F.; Paschos, O.; Maglia, F.; Lupart, S.; Lamp, P.; Giordano, L.; Shao-Horn, Y. Inorganic Solid-State Electrolytes for Lithium Batteries: Mechanisms and Properties Governing Ion Conduction. *Chem. Rev.* **2016**, *116*, 140–162.

(18) Kamaya, N.; Homma, K.; Yamakawa, Y.; Hirayama, M.; Kanno, R.; Yonemura, M.; Kamiyama, T.; Kato, Y.; Hama, S.; Kawamoto, K.; Mitsui, A. A Lithium Superionic Conductor. *Nat. Mater.* **2011**, *10*, 682–686.

(19) Hori, S.; Kato, M.; Suzuki, K.; Hirayama, M.; Kato, Y.; Kanno, R. Phase Diagram of the Li_4GeS_4-Li_3PS_4 Quasi-Binary System Containing the Superionic Conductor $Li_{10}GeP_2S_{12}$. *J. Am. Ceram. Soc.* **2015**, *98*, 3352–3360.

(20) Wenzel, S.; Randau, S.; Leichtweiß, T.; Weber, D. A.; Sann, J.; Zeier, W. G.; Janek, J. Direct Observation of the Interfacial Instability of the Fast Ionic Conductor $Li_{10}GeP_2S_{12}$ at the Lithium Metal Anode. *Chem. Mater.* **2016**, *28*, 2400–2407.

(21) Deng, Y.; Eames, C.; Chotard, J.-N.; Lalère, F.; Seznec, V.; Emge, S.; Pecher, O.; Grey, C. P.; Masquelier, C.; Islam, M. S. Structural and Mechanistic Insights into Fast Lithium-Ion Conduction in Li_4SiO_4-Li_3PO_4 Solid Electrolytes. *J. Am. Chem. Soc.* **2015**, *137*, 9136–9145.

(22) Li, Y.; Zhou, W.; Chen, X.; Lü, X.; Cui, Z.; Xin, S.; Xue, L.; Jia, Q.; Goodenough, J. B. Mastering the Interface for Advanced All-Solid-State Lithium Rechargeable Batteries. *Proc. Natl. Acad. Sci. U. S. A.* **2016**, *113*, 201615912.

(23) Kumar, B.; Thomas, D.; Kumar, J. Space-Charge-Mediated Superionic Transport in Lithium Ion Conducting Glass–Ceramics. *J. Electrochem. Soc.* **2009**, *156*, A506.

(24) Sandomirskii, P. A.; Simonov, M. A.; Belov, N. V. Crystal structure of the mixed lithium zinc orthophosphate $Li_4Zn[PO_4]_2$. *Dokl. Akad. Nauk SSSR* **1976**, *228,* 344.

(25) Torres-Treviño, G.; West, A. R. Compound Formation, Crystal Chemistry, and Phase Equilibria in the System Li_3PO_4-$Zn_3(PO_4)$. *J. Solid State Chem.* **1986**, *66*, 56–66.

(26) Torres-Treviño, G.; West, A. R. Thermodynamic, Kinetic, and Conductivity Studies of an Order-Disorder Transition in $Li_4Zn(PO_4)_2$. *J. Solid State Chem.* **1987**, *71*, 380–383.

(27) Jensen, T. R.; Hazell, R. G.; Christensen, A. N.; Hanson, J. C. Hydrothermal Synthesis of Lithium Zinc Phosphates: Structural Investigation of Twinned α-$Li_4Zn(PO_4)_2$ and a High Temperature Polymorph β-$Li_4Zn(PO_4)_2$. *J. Solid State Chem.* **2002**, *351*, 341–351.

(28) Liu, Z.; Fu, W.; Payzant, E. a; Yu, X.; Wu, Z.; Dudney, N. J.; Kiggans, J.; Hong, K.; Rondinone, a J.; Liang, C. Anomalous High Ionic Conductivity of Nanoporous β-Li_3PS_4. *J Am Chem Soc* **2013**, *135*, 975–978.

(29) Anantharamulu, N.; Koteswara Rao, K.; Rambabu, G.; Vijaya Kumar, B.; Radha, V.; Vithal, M. A Wide-Ranging Review on Nasicon Type Materials. *J. Mater. Sci.* **2011**, *46*, 2821–2837.

(30) Thangadurai, V.; Narayanan, S.; Pinzaru, D. Garnet-Type Solid-State Fast Li Ion Conductors for Li Batteries: Critical Review. *Chem. Soc. Rev.* **2014**, *43*, 4714–4727.

(31) Takada, K.; Osada, M.; Ohta, N.; Inada, T.; Kajiyama, A.; Sasaki, H.; Kondo, S.; Watanabe, M.; Sasaki, T. Lithium Ion Conductive Oxysulfide, Li_3PO_4–Li_3PS_4. *Solid State Ionics* **2005**, *176*, 2355–2359.

(32) Kumar, P. J.; Nishimura, K.; Senna, M.; Düvel, A.; Heitjans, P.; Kawaguchi, T.; Sakamoto, N.; Wakiya, N.; Suzuki, H. A Novel Low-Temperature Solid-State Route for Nanostructured Cubic Garnet $Li_7La_3Zr_2O_{12}$ and Its Application to Li-Ion Battery. *RSC Adv.* **2016**, *6*, 62656–62667.

(33) Thangadurai, V.; Pinzaru, D.; Narayanan, S.; Baral, A. K. Fast Solid-State Li Ion Conducting Garnet-Type Structure Metal Oxides for Energy Storage. *J. Phys. Chem. Lett.* **2015**, *6*, 292–299.

(34) Wu, J.-F.; Chen, E.-Y.; Yu, Y.; Liu, L.; Wu, Y.; Pang, W. K.; Peterson, V. K.; Guo, X. Gallium-Doped $Li_7La_3Zr_2O_{12}$ Garnet-Type Electrolytes with High Lithium-Ion Conductivity. *ACS Appl. Mater. Interfaces* **2017**, *9*, 1542–1552.

(35) Afyon, S.; Krumeich, F.; Rupp, J. L. M. A Shortcut to Garnet-Type Fast Li-Ion Conductors for All-Solid State Batteries. *J. Mater. Chem. A* **2015**, *3*, 18636–18648.

(36) Boultif, A.; Louer, D. Indexing of Powder Diffraction Patterns for Low-Symmetry Lattices by the Successive Dichotomy Method. *J. Appl. Cryst.* **1991**, *24*, 987–993.

(37) Rodríguez-Carvajal, J. *FullProf Suite; All Programs Can Be Obtained from: http://www.ill.eu/sites/fullprof.*

(38) Adams, S. From Bond Valence Maps to Energy Landscapes for Mobile Ions in Ion-Conducting Solids. *Solid State Ionics* **2006**, *177*, 1625–1630.

(39) Lander, L.; Reynaud, M.; Rousse, G.; Sougrati, M. T.; Laberty-Robert, C.; Messinger, R. J.; Deschamps, M.; Tarascon, J.-M. Synthesis and Electrochemical Performance of the Orthorhombic $Li_2Fe(SO_4)_2$ Polymorph for Li-Ion Batteries. *Chem. Mater.* **2014**, *26*, 4178–4189.

(40) Irvine, J. T. S.; Sinclair, D. C.; West, A. R. Electroceramics: Characterization by Impedance Spectroscopy. *Adv. Mater.* **1990**, *2*, 132–138.

(41) Phani Dathar, G. K.; Balachandran, J.; Kent, P. R. C.; Rondinone, A. J.; Ganesh, P. Li-Ion Site Disorder Driven Superionic Conductivity in Solid Electrolytes: A First-Principles Investigation of β-Li_3PS_4. *J. Mater. Chem. A* **2017**, *5*, 1153–1159.

(42) Jacquet, Q.; Perez, A.; Batuk, D.; Van Tendeloo, G.; Rousse, G.; Tarascon, J. M. The $Li_3Ru_yNb_{1-y}O_4$ (0 ≤y ≤1) System: Structural Diversity and Li Insertion and Extraction Capabilities. *Chem. Mater.* **2017**, *29*, 5331–5343.

(43) Imashuku, S.; Uda, T.; Nose, Y.; Kishida, K.; Harada, S.; Inui, H.; Awakura, Y. Improvement of Grain-Boundary Conductivity of Trivalent Cation-Doped Barium Zirconate Sintered at 1600°C by Co-Doping Scandium and Yttrium. *J. Electrochem. Soc.* **2008**, *155*, B581.

(44) Avila-Paredes, H. J.; Choi, K.; Chen, C.-T.; Kim, S. Dopant-Concentration Dependence of Grain-Boundary Conductivity in Ceria: A Space-Charge Analysis. *J. Mater. Chem.* **2009**, *19*, 4837.

Table of Contents